DEVELOPMENTAL NEUROSCIENCE

Shaping early neural development by timed elevated tissue oxygen tension: Insights from multiomic analysis on human cerebral organoids

Yuan-Hsuan Liu[1], Meng-Ting Chung[1], Hsi-Chieh Lin[1], Tse-Ang Lee[1], Ya-Jen Cheng[2,3], Chien-Chang Huang[4], Hsiao-Mei Wu[1,5]*, Yi-Chung Tung[1]*

Oxygen plays a critical role in early neural development in brains, particularly before establishment of complete vasculature; however, it has seldom been investigated due to technical limitations. This study uses an in vitro human cerebral organoid model with multiomic analysis, integrating advanced microscopies and single-cell RNA sequencing, to monitor tissue oxygen tension during neural development. Results reveal a key period between weeks 4 and 6 with elevated intra-organoid oxygen tension, altered energy homeostasis, and rapid neurogenesis within the organoids. The timed oxygen tension elevation can be suppressed by hypoxia treatment or silencing of neuroglobin gene. This study provides insights into the role of oxygen in early neurogenesis from functional, genotypic, phenotypic, and proteomic aspects. These findings highlight the significance of the timed tissue oxygen tension elevation in neurogenesis and provide insights into the role of neuroglobin in neural development, with potential implications for understanding neurodegenerative diseases and therapeutic strategies.

INTRODUCTION

Oxygen plays a critical role in cell metabolism, and its availability can greatly influence the development of cells, maturity, and homeostasis, particularly in the case of the brain. Despite accounting for only 2% of total body weight in a human, the brain consumes nearly 20% of total body oxygen (*1*). This highlights the importance of oxygen in early neural development. To better explore the roles of oxygen, oxygen tension, referring to the level of oxygen present in a specific environment, in a biological system is often characterized. Research has shown that low oxygen tension during the early stages of gestation can lead to symmetric division of radial glial cells (RGCs) in a fetal brain, which expands the stem cell population (*2*). As development progresses, angiogenesis occurs and blood vessels extend into the brain to supply oxygen and nutrients (*3*). During the establishment of functional neural circuits, adequate oxygenation drives metabolic changes, providing the energy required for neuronal differentiation and maturation (*2*). When optimal oxygen levels are deviated, it can result in neurodevelopmental disorders leading to severe outcomes including cerebral palsy, epilepsy, cognitive impairments, and even death (*4*). Furthermore, manipulating oxygen levels during pregnancy has been shown to have great impact on neurogenesis in offspring (*5*). Consequently, properly timed oxygen tension variation within the tissue is crucial for early neural development.

Given the significance of oxygen, measurement of tissue oxygen tension variation throughout the neural development process can provide insightful information for neuron science research. However, direct monitoring of human brain development in vivo is challenging due to technical limitations. As a solution, human cerebral organoids (hCOs) have been developed as an in vitro model system to study the progress of neural development and disorders in human brains (*6*). The hCOs, derived from human embryonic stem cells (hESCs) or human induced pluripotent stem cells (hiPSCs), are capable of reconstituting in vivo three-dimensional cell arrangements and can also recapitulate functional neural activity and gene expression profiles similar to a human brain (*6*–*8*). Therefore, the hCO has great potential for biomedical studies and provides a valuable tool for investigating the oxygen variation in neural development (*6*, *9*–*13*).

Various approaches have been developed to monitor the oxygen tension within the hCOs. For instance, a needle-type optical fiber microsensor has been exploited to monitor the intra-organoid oxygen tension for neurological disease studies (*11*). The detection scheme provides spatial oxygen tension profile variation in the hCOs; however, the invasive measurement process makes it impractical to measure live samples over an extended period (in orders of weeks) during the neuronal development process. Therefore, noninvasive optical detection techniques have been developed for the intra-organoid oxygen tension measurement. For consistent measurement with minimal interference from the ambient environment, measurements based on oxygen-sensitive dyes or particles with lifetime-based microscopy such as phosphorescence lifetime microscopy (PLIM) and fluorescence lifetime imaging microscopy (FLIM) have been exploited (*14*, *15*). However, the conventional time-domain lifetime measurement often requires high excitation light dosage, leading to photocytotoxicity, which makes it disadvantageous for live organoid observation over an extended period. Without consistent oxygen tension measurement in a time-lapse manner and extensive cell analysis, it is infeasible to monitor oxygen variation within tissues and decipher its role in neural development.

In this research, we construct a cerebral model and perform time-lapse intra-organoid oxygen tension measurements using the ruthenium-based oxygen-sensitive fluorescence microbeads

[1]Research Center for Applied Sciences, Academia Sinica, Taipei, Taiwan. [2]Institute of Molecular Biology, Academia Sinica, Taipei, Taiwan. [3]Neuroscience Program of Academia Sinica, Academia Sinica, Taipei, Taiwan. [4]SYNCELL Inc., Taipei, Taiwan. [5]Department of Biomechatronics Engineering, National Taiwan University, Taipei, Taiwan.
*Corresponding author. Email: hsmwu@ntu.edu.tw (H.-M.W.); tungy@gate.sinica.edu.tw (Y.-C.T.)

and frequency domain FLIM (FD-FLIM). With the widefield capability, FD-FLIM provides rapid fluorescence lifetime measurement with minimum excitation light dosage and excellent immunity to ambient optical noise, making it feasible for long-term monitoring. Therefore, we can accurately estimate the oxygen tension from the measured lifetime values as a functional assay. Furthermore, we take advantage of multiomic analysis approach, integrating confocal microscopy and single-cell RNA sequencing (scRNA-seq), to investigate cellular responses during the early neural development based on the hCO model (Fig. 1A). Imaging the sectioned samples using confocal microscopy, the structure and expression of marker proteins of the hCOs can be observed. In addition, the scRNA-seq can provide us the cells' detailed composition and evolution from the transcriptomic profiles. With the observed functional (intra-organoid oxygen tension), genotypic, phenotypic, and proteomic information provided by the multiomic analysis, we identify a specific period with elevated oxygen tension (weeks 4 to 6) that is critical for early neural development.

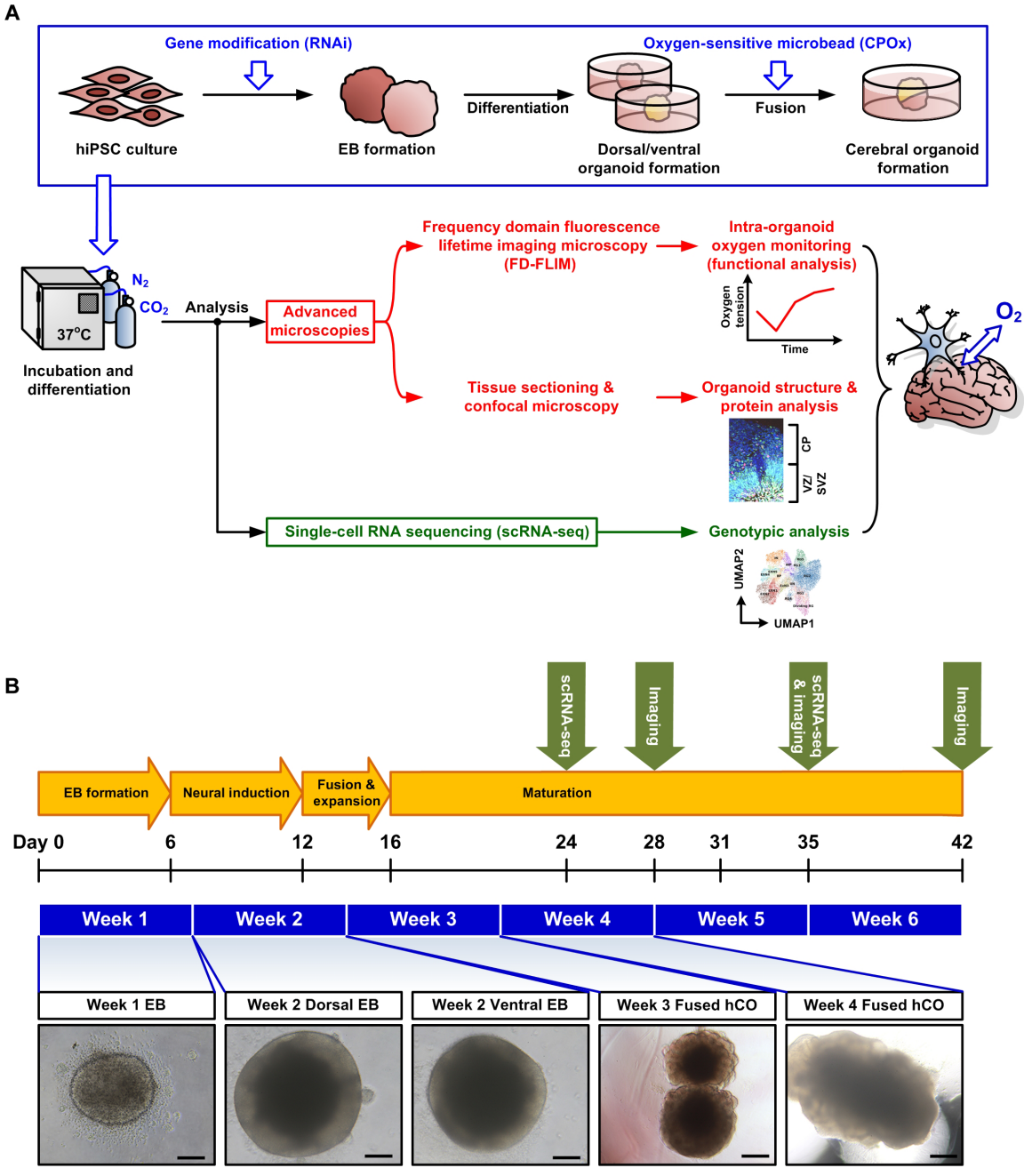

Fig. 1. Multiomic analysis on hCOs. (**A**) Schematic of the approach integrating advanced microscopy and scRNA-seq to measure the intra-organoid oxygen tension variation and its impact on the cellular response throughout the early central neuron system development process based on the cerebral organoid model. (**B**) Timeline of hCO formation and culture based on the fused cerebral organoid method, with all measurement points for data analysis denoted. Bright-field images of the control hCOs at different time points. Scale bars, 200 μm for weeks 1 and 2, and 500 μm for weeks 3 and 4.

RESULTS

Intra-organoid oxygen tension measurement on hCOs using FD-FLIM

To construct an in vitro model capable of modeling inter-regional interactions in a brain, a fused cerebral organoid formation approach is exploited in this research (*16*). The hiPSCs are first differentiated into dorsal and ventral cerebral organoids separately. The two organoids are then fused within a hydrogel substrate to form an hCO with multiple distinct region identities in a controlled manner (*16*) (Fig. 1B). To evaluate the organoid growth and development, we estimate the sizes of the hCOs with the embedded 50-μm-diameter oxygen-sensitive fluorescence microbeads (CPOx, Colibri Photonics GmbH) from the captured microscopic images (Fig. 2A) by quantifying areas occupied by the hCOs. Figure 2B shows the size distributions of the hCOs at weeks 4 to 6, indicating that the average spheroid sizes (areas) increased by approximately 35.3% and 19.7%

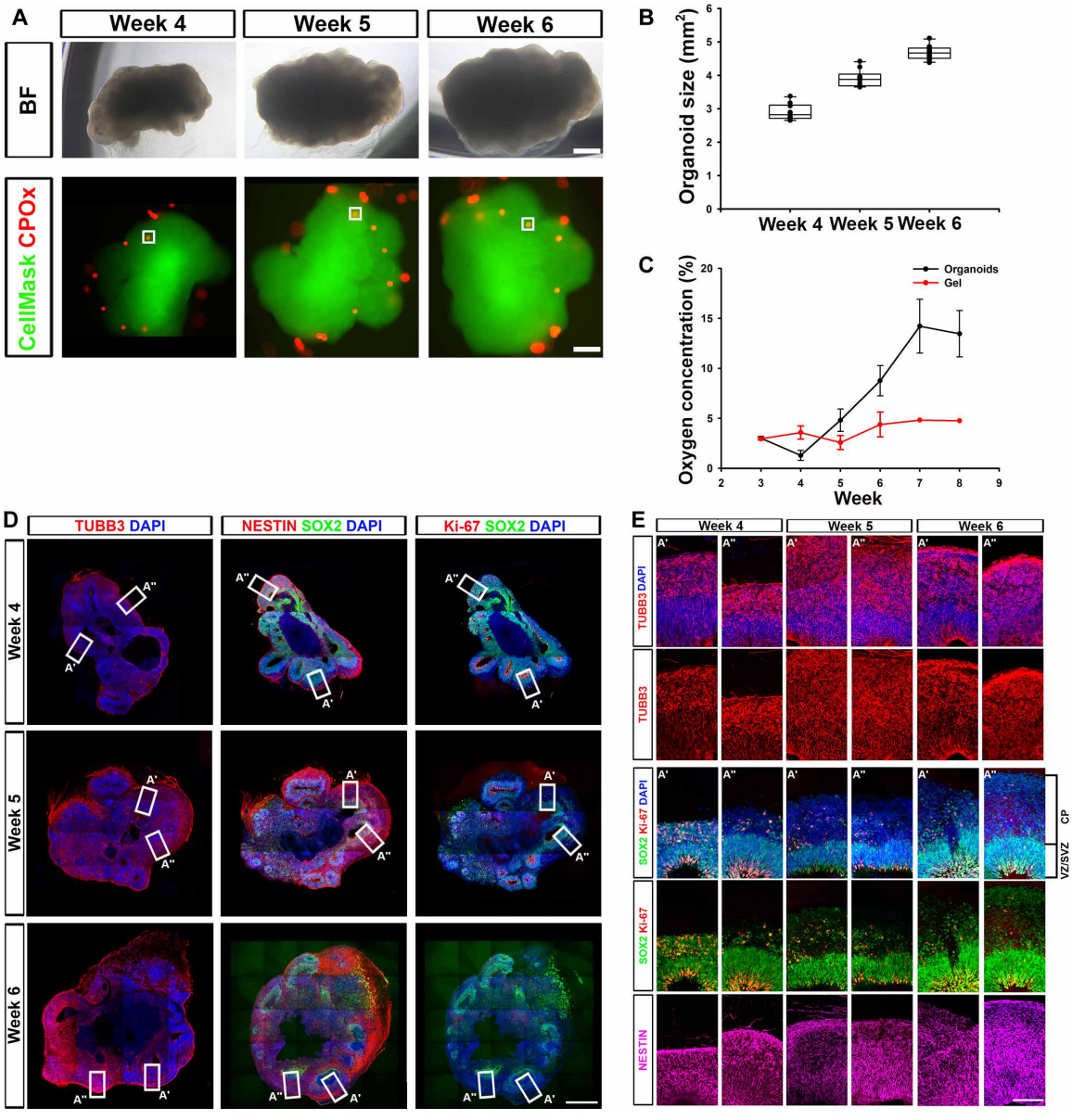

Fig. 2. Intra-organoid oxygen tension, structure, and cell compositions of hCOs. (**A**) Bright-field images of the control hCOs cultured in the hydrogel matrix at different time points (scale bar, 400 μm), and fluorescence images of the control hCOs stained with a plasma membrane stain, CellMask (green), and the embedded oxygen-sensing CPOx beads (red) (scale bar, 400 μm). The representative CPOx beads embedded within the hCOs are denoted by white line squares. (**B**) Organoid sizes of the hCOs estimated from the captured bright-field images. Data are presented as box plots with all data points and mean (SD) ($n = 10$). (**C**) Quantitative results of the average oxygen tension values calculated based on the fluorescence lifetime measurement of CPOx beads embedded within the hCOs (intra-organoid oxygen tension) or within the hydrogel but not embedded within the hCOs (hydrogel oxygen tension). The data are expressed as mean (SD). The quantitative data are shown in table S2. (**D**) Confocal images of hCO slices stained with TUBB3, SOX2, Nestin, and Ki-67 proteins and cell nuclei [4′,6-diamidino-2-phenylindole (DAPI)] reveal the distribution of neurons and NSCs in the hCOs at weeks 4 to 6 (scale bar, 400 μm). (**E**) Zoom-in confocal images presenting the selected A′ and A″ regions (white squares) within the hCOs at weeks 4 to 6 as those are originally depicted in (D) (scale bar, 100 μm).

during the fourth and fifth week of the culture, respectively. The observed size increase is similar to that reported in previous literatures, indicating the rapid expansion in the early neurogenesis in hCOs during a specific developing time window (*5*). The results confirm the feasibility and robustness of our experimental approach for the intra-organoid measurement. We also confirm that the microbeads can be well distributed in the hCOs and hydrogels (fig. S1A), and the introduction of the microbeads into hCOs has minimal effects on neural development within the organoids based on the microscopic image observation (fig. S1B) and quantitative structural characterization (fig. S1E).

It has been reported that oxygen tension plays a critical role in regulating the proliferation of neural stem/progenitor cells and neuronal differentiation, which ultimately influences the size of the brain during developmental stages (*5*, *17*, *18*). Exploiting the oxygen-sensitive fluorescence microbeads (CPOx) with the FD-FLIM setup, we can monitor the intra-organoid oxygen tension variation during the specific time window. Since it takes 2 weeks to grow the fused hCO with initial tissue-like structures from the hiPSCs, the intra-organoid oxygen tensions within the hCOs are measured from week 3. The oxygen tension variations are observed for more than 6 weeks; the results are shown in Fig. 2C.

Under the normal culture condition, the average intra-organoid oxygen tension is estimated to be 3.0 ± 0.9% at week 3, and it decreases to the lowest value of 1.9 ± 0.3% at week 4. Interestingly, the oxygen tension elevates after week 4, reaching the highest value of approximately 14.2% at week 7. To ensure the minimal effects from the ambient environment on oxygen tension measurements, the oxygen tensions within the hydrogel in which the hCO is cultured are also characterized. The measured oxygen tension values are relatively constant and vary between 3.5% and 4.8% from week 3 to 8, suggesting the consistent measurement using the developed approach. The results indicate that the intra-organoid oxygen tensions are mainly regulated by cellular activities during the hCO development.

Confocal microscopy for structure characterization

Here, we use confocal microscopy in the experiments to gain insights into the cell arrangement and structural change within the hCOs during the specific period with the elevated oxygen tension. The hCOs are fluorescently stained with markers of differentiated neurons (TUBB3) and neural stem cells (NSCs) (NESTIN, SOX2, and Ki-67) to observe the process of neurogenesis (Fig. 2D). Both thicknesses and the cell populations of the developing neuroepithelia regions with ventricular zone/subventricular zone–like (VZ/SVZ) and cortical plate–like (CP) structures are analyzed from the fluorescence images (Fig. 2E) following the established methodologies detailed in the literatures (*19*–*21*). The quantitative results reveal that the VZ/SVZ maintains a consistent thickness during the specific period of elevated oxygen tension (fig. S2A), while the CP region exhibits an increase of approximately 79.8% in thickness (fig. S2B).

Specifically, the $TUBB3^+$ cells indicating differentiated neurons are primarily localized in the CP and constitute 34.7 ± 4.1%, 51.5 ± 2.4%, and 53.3 ± 1.4% of the entire cell population at weeks 4, 5, and 6, respectively (fig. S2C). These results imply that the enlarged thickness of the CP region results from the increased neuronal population during the period with the elevated intra-organoid oxygen tension. In contrast, the $SOX2^+$ cells representing NSCs are predominantly localized in the VZ/SVZ and comprise 62.6 ± 7.6%, 44.7 ± 4.0%, and 47.8 ± 3.7% of the entire populations at weeks 4, 5, and 6, respectively (fig. S2D). Furthermore, the proliferating cells indicated by Ki-67 staining are also mainly found in the VZ/SVZ. The ratios of proliferating cells are 22.4 ± 2.5%, 15.4 ± 1.9%, and 13.2 ± 4.1% in weeks 4, 5, and 6, respectively (fig. S2E). Together, these results suggest that elevated oxygen tension is associated with a shift in neurogenesis dynamics, favoring the generation of neurons within the hCOs for rapid expansion during this specific period.

Regulation of neurogenesis in hCOs by oxygen tension elevation

To uncover the crucial role of the elevated oxygen tensions at specific developmental periods, we exposed the hCOs to a hypoxic environment (5% O_2) for 3 days in week 4 to reduce oxygen supply from the ambient. The intra-organoid oxygen tensions and the growth of the hypoxia-treated hCOs are observed, as shown in Fig. 3. The observed average size of the hypoxia-treated hCOs shows a remarkable reduction compared to the control group at weeks 5 and 6 (Fig. 3, A and B). In addition, the intra-organoid oxygen tension is measured at 1.8 ± 0.9% during the hypoxia treatment period, a level significantly lower than that observed in the control group. Although oxygen tension elevation is observed right after the hypoxic treatment, the oxygen tension is quickly flattened for the hypoxia-treated hCOs, showing a sustained low oxygen level beyond week 5 (Fig. 3C). It is noted that the effects of lower oxygen tension (1% O_2) or prolonged hypoxia treatment have also been explored in our experiments. However, the structural integrity of the hCOs has been compromised, and the growth of the organoids is seriously affected.

Regarding the organoid structure, the significant lower thickness of the CP-like region is observed in the hypoxia-treated hCOs (Fig. 3, D to F). In addition, hypoxia-treated hCOs exhibit a lower $TUBB3^+$ cell population at week 5 compared to the control ones (Fig. 3G). This reduction in the $TUBB3^+$ cell population contributes to the observed thinner CP-like region. In contrast, a higher $SOX2^+$ cell population and a lower $Ki\text{-}67^+$ cell population are observed in the hypoxia-treated hCOs at week 5 (Fig. 3G). With similar thickness observed in the VZ/SVZ-like region compared to the control ones (Fig. 3F), these results indicate a preference for NSCs to maintain a quiescent state in the hypoxia-treated hCOs. The results show that the reduced oxygen supply in the cellular microenvironment can affect the intra-organoid oxygen tension, leading to a reduction of organoid growth and the neurogenesis of the hCOs. These findings highlight the critical roles of optimal oxygen tension during the specific developmental period within the hCOs.

scRNA-seq analysis of hCOs and identification of potential oxygen-carrier genes

To explore the transcriptomic profile evolution of the hCOs cultured in the experiments, we introduce the scRNA-seq to perform on the hCOs on days 24 and 35 to compare the changes before and after the period with the elevated intra-organoid oxygen tension (*22*). The transcriptomic profiles at two time points are first combined and visualized as a heatmap (Fig. 4A) and a Uniform Manifold Approximation and Projection (UMAP) plot (Fig. 4B). The cell population can be segmented into 15 clusters containing four major cell types: radial glial (RG) cells, excitatory neuron (EXN), progenitor of interneuron (INP), and interneuron (IN) based on the representative markers described in previous literatures (*7*, *23*).

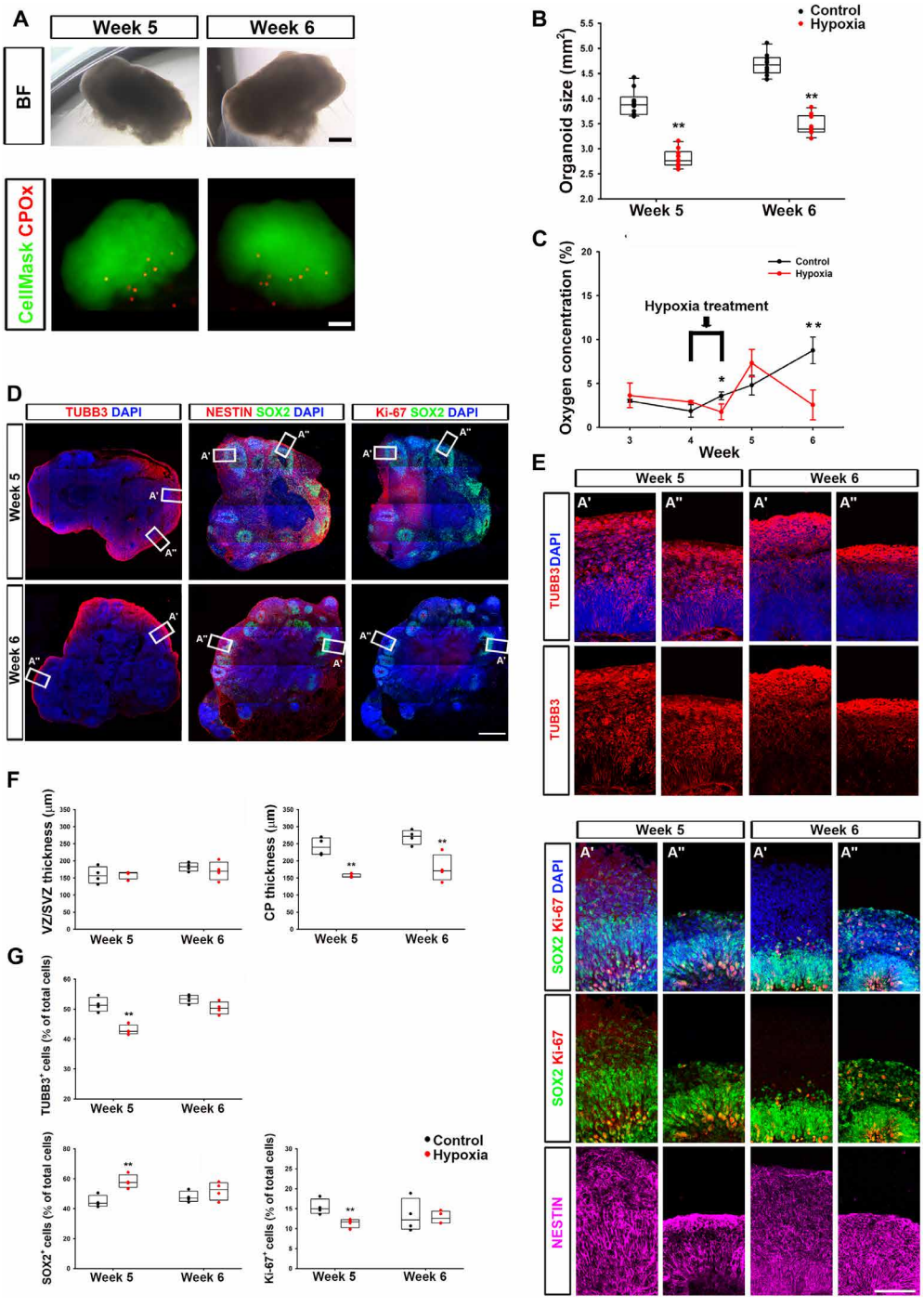

Fig. 3. Intra-organoid oxygen tension, structures, and cell compositions of hypoxia-treated hCOs. (**A**) Bright-field images of the hypoxia-treated hCOs cultured in the hydrogel matrix at different time points (scale bar, 400 μm), and fluorescence images of the hypoxia-treated hCOs stained with a plasma membrane stain, CellMask (green), and the embedded oxygen-sensing CPOx beads (red) (scale bar, 400 μm). (**B**) Comparison of the organoid size of the control and hypoxia-treated hCOs estimated from the captured bright-field images. Data are presented as box plots with all data points and mean (SD) ($n = 10$). (**C**) Comparison of the average oxygen tension values calculated based on the fluorescence lifetime measurement of CPOx beads embedded within the control and hypoxia-treated hCOs (intra-organoid oxygen tension). (**D**) Confocal images of hypoxia-treated hCO slices stained with TUBB3, SOX2, Nestin, and Ki-67 proteins and cell nuclei (DAPI) revealing the distribution of neurons and NSCs in the hCOs at weeks 5 and 6, respectively (scale bar, 400 μm). (**E**) Zoom-in confocal images presenting the selected A′ and A″ regions (white square) within the hypoxia-treated hCOs at weeks 5 and 6 (scale bar, 100 μm) as originally depicted in (D). (**F**) Comparison of VZ/SVZ and CP region thicknesses in the hCOs (control and hypoxia-treated ones) at weeks 5 and 6. The thicknesses are analyzed from the captured fluorescence images ($n = 4$). (**G**) Comparison of TUBB3$^+$, SOX2$^+$, and Ki-67$^+$ cell numbers in the hCOs at weeks 5 and 6. The numbers are enumerated from the captured fluorescence images. One-way analysis of variance (ANOVA) with Tukey's test is performed for statistical analysis. Data are presented as box plots and mean (SD) with all data points ($n = 4$). All the quantitative data are shown in table S3.

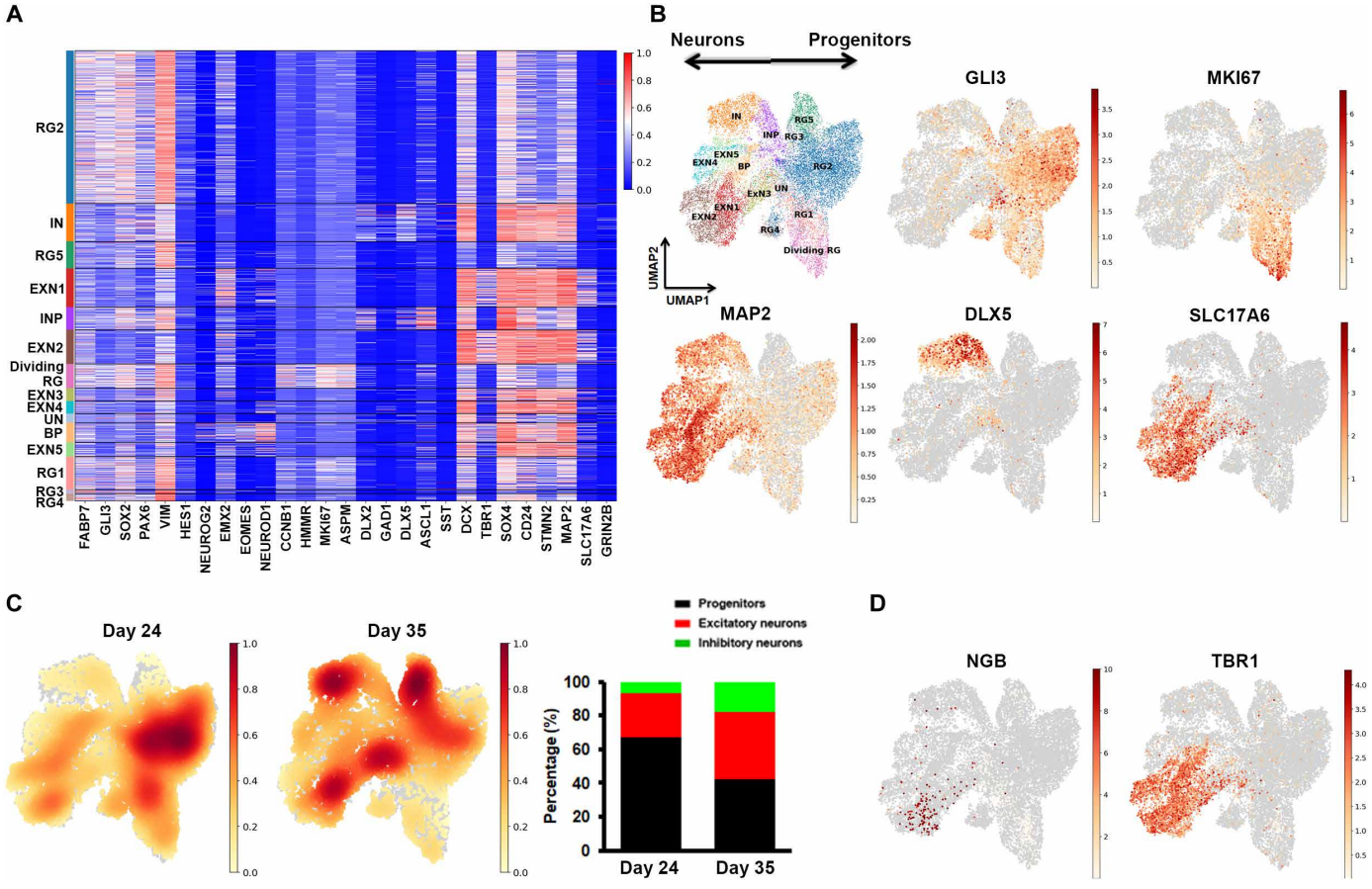

Fig. 4. Cell type identification in hCOs at days 24 and 35 using scRNA-seq. Total of 11,706 and 7187 transcriptomes of single cells within the hCOs at days 24 and 35 are combined for analysis, respectively. The data obtained from the hCO at day 35 are used as the reference. (**A**) Expression pattern of representative marker genes visualized by a heatmap. The distinct groups in the hCOs at days 24 and 35 are clustered into RGCs (RG1 to RG5), dividing RGCs (Dividing RG), basal progenitor cells (BP), excitatory neurons (EXN1 to EXN4), interneuron progenitor cells (INP), interneurons (IN), and undefined neurons (UN). (**B**) Combined data mapped into a UMAP plot and colored using the Leiden graph-clustering method. The expression patterns of particular marker genes (*GLI3*, *MKI67*, *MAP2*, *DLX5*, and *SLC17A6*) are also shown as UMAP plots. (**C**) Density plots showing the cell compositions within the hCOs at days 24 and 35. The quantitative results are plotted as bar graphs, and the data are shown in table S4. (**D**) Combined UMAP plots of the hCOs showing the cells expressing oxygen-carrier gene (*NGB*) and the marker gene (*TBR1*) of differentiated excitatory neurons.

The analysis results are further visualized as density plots, and a quantitative bar plot is used in Fig. 4C to observe the cell composition variation. The plots show that the hCO on day 24 mainly consists of RGCs (67.2%), bipolar-shaped progenitor cell types responsible for producing neurons in the cerebral cortex (*20*). The cells are then differentiated into excitatory neurons and interneurons on day 35. The transcriptomic profiles agree well with the captured fluorescence images (Fig. 2), showing the increased CP thickness during the culture. In addition, the gene sets responding to neural development, synaptic transmission, and axonogenesis are identified from the EnrichR database (fig. S3). The results confirm that the differentiated hCOs in the experiments are well organized.

To explore the possible oxygen-binding genes capable of regulating the intra-organoid oxygen tension of the hCOs, a query in the Gene Ontology (GO) database is performed (*24*, *25*). With great oxygen-binding capacity, the genes related to the globin family are promising candidates (table S1). Upon analyzing the scRNA-seq results obtained from the hCOs in the control experiments, neuroglobin (*NGB*), predominantly expressed in the central nervous system (CNS) (*26*, *27*), is pinpointed as a noteworthy candidate gene. The scRNA-seq results show that *NGB*-expressing cells mainly belong to excitatory neurons (EXN1 and EXN2 in Fig. 4D). Specifically, the *NGB*-expressing cells overlap with those expressing *TBR1*, indicating their identities as deep-layer cortical neurons in the hCOs at the early development stage.

Effects of *NGB* silencing on intra-organoid oxygen tension, hCO structure, and cell composition

To confirm the critical role of *NGB* and to explore its function for hCO development, short hairpin RNA (shRNA) is exploited to knock down the *NGB* expression of the hiPSCs for hCO formation. The analyses are performed on the formed *NGB* knockdown (shNGB) hCOs and the shLacZ control hCOs for comparison. Examining organoid sizes based on estimating the microscopic bright-field images (Fig. 5A) reveals that the average size of the shLacZ hCOs remains similar to those of the control ones (Fig. 5B). This observation suggests that using shRNA does not affect the normal development of hCOs. However, the sizes of the shNGB hCOs are 14 to 23% smaller than those of the control ones throughout the observation period (Fig. 5B), similar to the observations made in

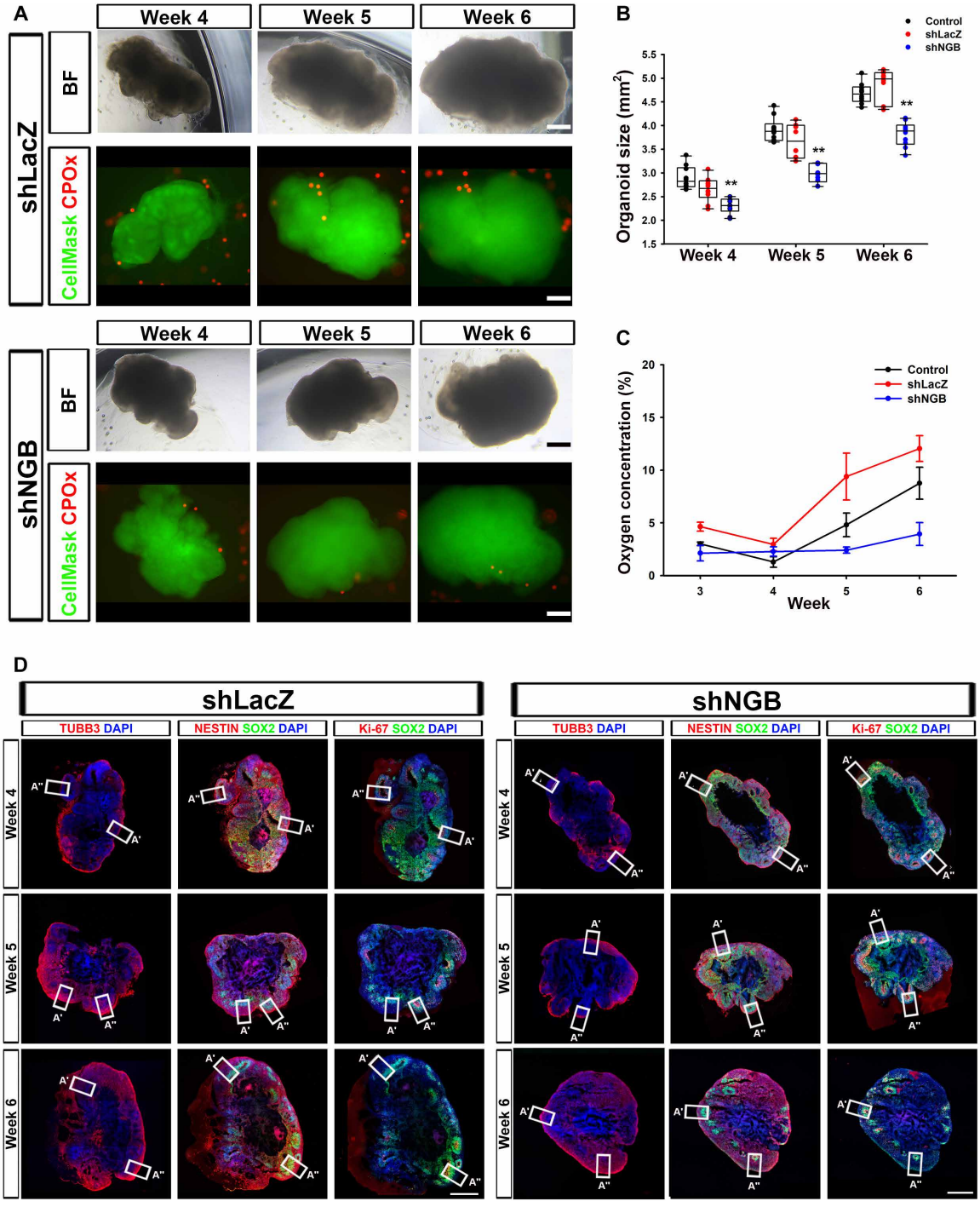

Fig. 5. Intra-organoid oxygen tension, structures, and cell compositions of shLacZ and NGB knockdown (shNGB) hCOs. (**A**) Bright-field images of the shLacZ and shNGB hCOs cultured in the hydrogel matrix at different time points (scale bar, 400 μm), and fluorescence images of the shLacZ and shNGB hCOs stained with CellMask (green) and the embedded oxygen-sensing CPOx beads (red) (scale bar, 400 μm). (**B**) Organoid sizes of the shLacZ and shNGB hCOs estimated from the captured bright-field images. Data are presented as box plots and mean (SD) with all data points. One-way ANOVA with Tukey's test is performed for statistical analysis ($n = 10$). (**C**) Comparison of the average oxygen tension values calculated based on the fluorescence lifetime measurement of CPOx beads embedded within the control, shLacZ, and shNGB hCOs (intra-organoid oxygen tension) at weeks 4 to 6. The data are expressed as mean (SD), and one-way ANOVA with Tukey's test is performed for statistical analysis. The quantitative data are shown in table S4. (**D**) Confocal images of shLacZ and shNGB hCOs slices stained with TUBB3, SOX2, Nestin, and Ki-67 proteins and cell nuclei (DAPI), revealing the distribution of neurons and NSCs in the hCOs at weeks 4 to 6 (scale bar, 400 μm).

hCOs subjected to hypoxia. The results imply that silencing of *NGB* may also affect the intra-organoid oxygen tension of the hCOs.

To test the implication, we measure the intra-organoid oxygen tension on the shLacZ and shNGB hCOs (Fig. 5A). The results show that the average oxygen tension profile of the shLacZ hCOs resembles that of the control hCOs with a slight elevation. In contrast, the oxygen tension in the shNGB hCOs is flattened at a relatively low level, with values constantly below 5% (Fig. 5C). Although the role of NGB in the oxygenation of the CNS remains unclear and has been seldom explored (*28*, *29*), our findings provide direct evidence that NGB contributes to the elevation of intra-organoid oxygen tension during a specific period. Considering the observations from the hypoxia treatment experiment, we confirm that both an adequate ambient oxygen supply and the presence of cells expressing *NGB* play critical roles in establishing the microenvironment with timed elevated oxygen tension in hCOs during the developmental process.

We further investigate the impact of the attenuated elevation in oxygen tension on the neuronal development of the shNGB hCOs. We first image the sectioned hCOs stained with the markers of differentiated neurons and NSCs (Fig. 5D), and the structures are further quantified based on the zoom-in fluorescence images (Fig. 6, A and B). In our results, similar organoid structures are observed between the control and shLacZ groups, indicating that using shRNA does not disturb the developmental process of hCOs. Moreover, compared to the control and shLacZ groups, the CP-like regions within the shNGB hCOs display a remarkably lower thickness at weeks 5 and 6 (Fig. 6C). Notably, at week 4, the CP-like region is barely detectable in the shNGB hCOs (Fig. 6C). In contrast, the thickness of the VZ/SVZ-like regions within the shNGB hCOs is significantly increased at week 4 (Fig. 6C).

From the fluorescence staining images, the population of $TUBB3^+$ cells is significantly reduced in the shNGB hCOs at weeks 4 to 6 (Fig. 6D), leading to the observed diminished thickness of the CP-like region. In contrast, the populations of $SOX2^+$ cells and $Ki\text{-}67^+$ cells are significantly increased in the shNGB hCOs at weeks 4 to 6 (Fig. 6, B and D) compared to those in the control and shLacZ hCOs. The larger NSC population in the shNGB hCOs results in an increase in the thickness of the VZ/SVZ-like regions at week 4.

Comparison of transcriptomic profiles of control and shNGB hCOs

The cell composition in *NGB* knockdown hCOs is also examined using the scRNA-seq analysis (fig. S4A). The analyzed density plots show a predominance of stem/progenitor and dividing cell populations on day 24 and 35 shNGB hCOs. While day 35 shNGB hCOs exhibit a higher population of excitatory neurons and interneurons than do day 24 shNGB hCOs, the population of the differentiated neurons remains lower than that of the control group (fig. S4B). Additionally, the expression of *HIF1A*, a pivotal gene associated with hypoxia, can be detected in the shNGB hCOs. Furthermore, the representative HIF1A-regulated hypoxia-related genes, including *PDK3*, *KLF6*, and *FAM162A*, are also detected in the shNGB hCOs, indicating that a chronic hypoxia environment is established (fig. S4C).

To comprehensively assess the impact of *NGB* silencing on cellular homeostasis, we conduct an integrated analysis by concatenating the scRNA-seq datasets from both control and shNGB groups. The datasets are subjected to the Gene Set Enrichment Analysis (GSEA) through the MSigDB database (*30*) to dissect associated signaling pathways. The query results are visualized as a heatmap, as shown in fig. S4D, and the quantification for the expression levels of gene sets related to cellular homeostasis. We compare the expression levels of gene sets as fold changes relative to the day 24 control group (fig. S4E). Since chronic hypoxic conditions have been found to cause a reduction in energy availability and inactivation of anabolic processes (*31*), we examine the gene sets associated with metabolic pathways. From the analyzed results, we observe similar levels of oxidative phosphorylation–related gene set that serves as the primary energy source for anabolism for both control and shNGB hCOs at day 24. Compared to the day 24 hCOs, the oxidative phosphorylation gene set level increases for the day 35 control hCOs. In contrast, a notable reduction in the oxidative phosphorylation gene set level is observed within the day 35 shNGB hCOs. The results indicate that silencing of *NGB* disturbs metabolic homeostasis during the hCO development.

Beyond its effect on the elevated oxygen tension, NGB is also involved in multiple cellular processes, including reducing excessive reactive oxygen species (ROS), regulating mitochondrial function, and preventing apoptosis, all of which contribute to maintaining cellular homeostasis (*32*–*34*). In addition, NGB is also linked to Wnt signaling, a pathway critical for promoting neurogenesis (*35*). To investigate how the aforementioned NGB-associated pathways influence the observed effects on metabolic homeostasis and neurogenesis in the shNGB hCOs, we examine the expression patterns of genes involved in these pathways. The results are visualized as a heatmap shown in fig. S5A, and the quantitative analysis reveals that expression levels of these pathway-related gene sets are comparable between control and shNGB hCOs at days 24 and 35 (fig. S5B). The results indicate that the *NGB* silencing has minimal effects on these pathways.

DISCUSSION

hCOs have been broadly applied to construct in vitro model systems mimicking physiological structures and biochemical responses of tissues. Despite lacking a vascular system, studies demonstrated that mature hCOs can be grown to millimeter-scale sizes with well-differentiated cellular structures (*6*, *11*, *16*) containing inner cores without significant oxygen tension drop from the organoid surfaces (*11*), which is very different from other submillimeter-sized organoids (e.g., tumor organoids) having hypoxia necrotic cores. Taking advantage of the developed integrated approach, we measure the intra-organoid oxygen tension of the hCO for an extended period (until week 8). We observe the low intra-organoid oxygen tension in the initial differentiation stage of an hCO with a smaller size. The observation is similar to the minor differentiated neurospheres with the sizes restricted to approximately 500 μm in diameter due to limited diffusion of oxygen supply (*36*). We can identify a period (weeks 4 to 6) during which the intra-organoid oxygen tension elevates along with the rapid growth of the hCO.

Here, we have identified a period with elevated intra-organoid oxygen tension for the hCOs, and we find increased neurogenesis during the period from observation of structural and cellular composition changes using confocal microscopy and scRNA-seq, respectively. From further analysis of the scRNA-seq data, we notice the increased expression levels of oxidative phosphorylation–related gene set in the day 35 control hCOs during the intra-organoid oxygen tension elevation, indicating that elevated energy generation is closely coupled with the elevation of oxygen tension. Our findings

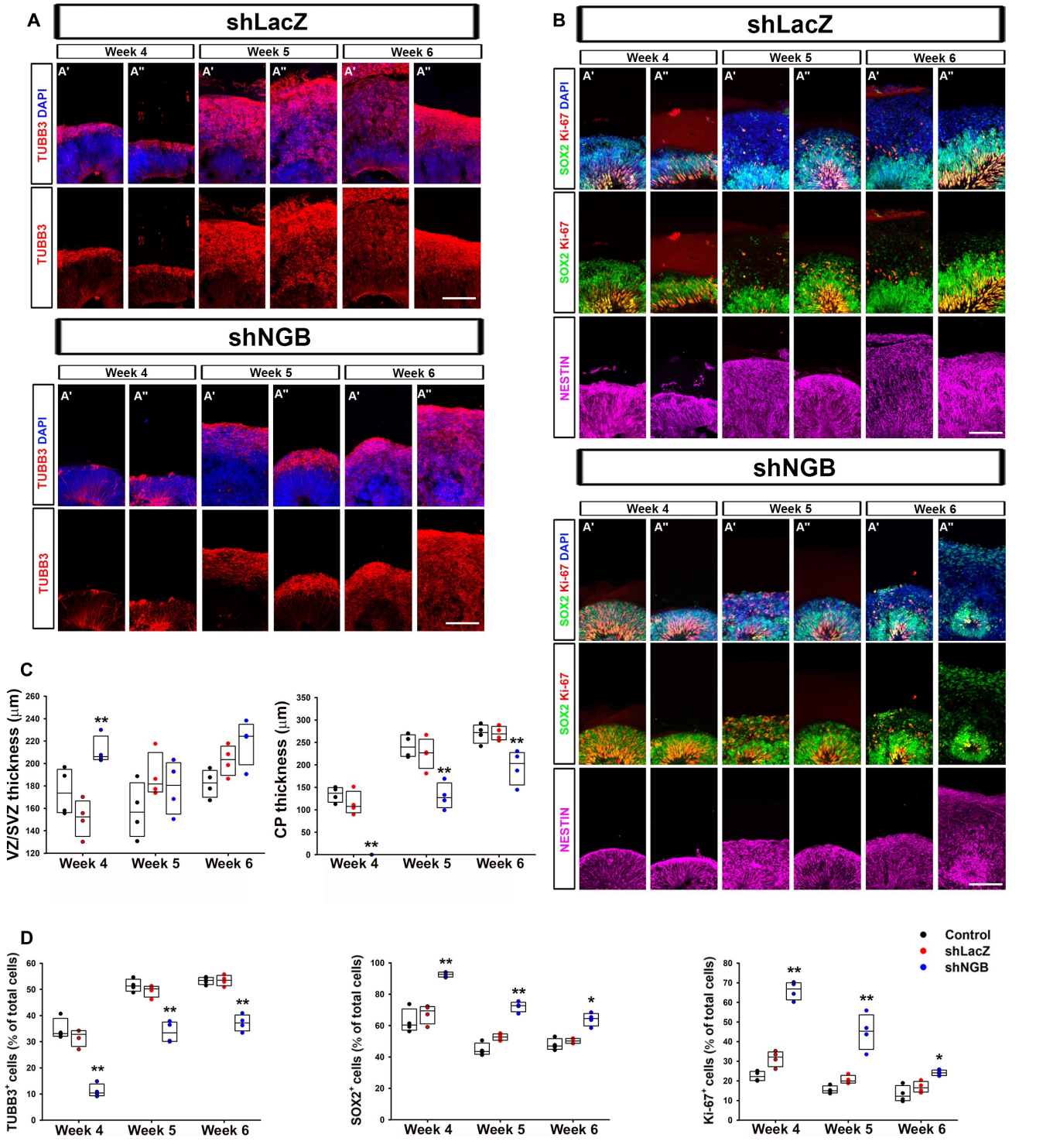

Fig. 6. Comparison of cells within control, shLacZ, and shNGB hCOs at weeks 4 to 6. (**A** and **B**) Zoom-in confocal images presenting the selected A′ and A″ regions (white squares) within the shLacZ and shNGB hCOs at weeks 4 to 6 as those are originally depicted in Fig. 5D. Scale bars, 100 μm. (**C**) Quantification of VZ/SVZ and CP region thicknesses in the hCOs analyzed from the captured fluorescence images at weeks 4 to 6 ($n = 4$). (**D**) Quantification of TUBB3$^+$, SOX2$^+$, and Ki-67$^+$ cells in the hCOs (control, shLacZ, and shNGB) analyzed from the captured fluorescence images at weeks 4, 5, and 6 weeks, respectively. One-way ANOVA with Tukey's test is performed for statistical analysis. Data are presented as box plots and mean (SD) with all data points ($n = 4$). The quantitative data are shown in table S5.

align with the previous study in which increased neuronal differentiation was observed during oxygenation periods in the developing cerebral cortex (*2*). Moreover, given the crucial role of oxygen in anabolism, the increased oxygen level has been reported to be essential for generating adenosine triphosphate (ATP) to support differentiation and maturation of neuronal cells during neurogenesis (*31*, *37*). Together, our results establish a direct correlation between increased energy demands and increased neurogenesis during periods of elevated oxygen tension and offer valuable insights into the physiological processes governing the development of the cerebral cortex.

Using the integrated approach, we further identify that both hypoxia treatment and the silencing of *NGB* can significantly attenuate intra-organoid oxygen tension elevation and consequently impair normal neurogenesis within the hCOs. The establishment of a chronic hypoxia microenvironment is further confirmed in the *NGB*-silencing hCO. The measured intra-organoid oxygen tensions, the observed organoid structures, and cell compositions agree well with the reported crucial roles of oxygen switch in coordinating the transition from NSCs expansion to neuronal differentiation during the early developmental cerebral cortex (*2*, *5*).

While vascular ingrowth undoubtedly plays a critical role in oxygen transportation and supply, previous research has shown other possible mechanisms for oxygen transportation. For example, it has been shown that vascular-deficient embryos contain lower tissue oxygenation than control ones, leading to a reduction of neurogenesis in the developing cerebral cortex (*2*). Interestingly, the elevated ambient oxygen can still be transported into the vascular-deficient embryos to relieve the hypoxic environment, resulting in the restoration of impaired neurogenic processes. In our hCO model, the mechanisms of oxygen transportation without involving the vessels may take a leading role in oxygenating the organoid and further promoting neurogenesis. The observation from the experiments in this study reveals how the nervous system can autonomously transport oxygen, which may provide a reasonable explanation for the relatively large size of the hCO compared to other types of organoids (e.g., neurospheres and tumor organoids). Furthermore, these results can pave the way to better explore early CNS development even without a sound vascular network in a brain.

To further investigate the possible oxygen transportation mechanism, we identify *NGB* as a key gene according to the scRNA-seq analysis results performed on the hCOs in this study. NGB, belonging to the globin family, is a previously undiscovered protein primarily found in neurons in 2000 (*28*, *38*). Its primary function includes neuroprotection, safeguarding neurons from damage and cell death caused by various forms of stress or injury (*39*, *40*). Interestingly, previous studies highlight the potential roles of abundantly expressed *NGB* in the retina for oxygen supply (*41*, *42*). Here, we observe a concentrated expression pattern of *NGB* in the $TBR1^+$ excitatory neurons of the hCOs.

Remarkably, silencing *NGB* leads to attenuated intra-organoid oxygen tension elevation without noticeable direct effects on expression of the neurogenesis-related genes. The observed flattened oxygen tension disrupts metabolic homeostasis and subsequently affects functional activities, including neurogenesis. Since oxygen provides critical energy for neural development, our study confirms the essential role of *NGB* in regulating intra-organoid oxygen tension. Our findings can provide a reasonable explanation for phenomena observed in previous studies. For example, it has been reported that the expression level of *NGB* in the embryonic brain undergoes a progressive increase through various developmental stages, persisting at high levels until postnatal stages (*27*, *43*). Moreover, *NGB* expression is also found to rise during neuronal differentiation (*44*), indicating a potential role for NGB in regulating neurogenesis throughout the developmental process. Together, our findings pave a path to explore the roles of NGB in regulating neurogenesis within the developing cerebral cortex through its function of regulating oxygen. This adds a dimension to our understanding of the multifaceted functions of NGB in neural development and oxygen homeostasis.

In summary, we measure intra-organoid oxygen tension in the hCOs for an extended period using oxygen-sensitive microbeads and FD-FLIM. On the basis of the measurement results, we identify a critical period with the elevated oxygen tension between weeks 4 and 6. Using the developed integrated multiomic analysis approach, we can investigate the pivotal role of the timed oxygen tension elevation in hCO development and its impact on neurogenesis. The research identifies that elevated oxygen tension can influence both neurogenesis and hCO growth. Furthermore, *NGB*, an essential gene primarily expressed in excitatory neurons, is critical in regulating oxygen tension within the hCOs. Silencing *NGB* attenuates intra-organoid oxygen tensions, further hinders organoid development, and alters cell composition. In addition, the experimental results confirm the functionalities of the integrated multiomic approach combining advanced microscopies and scRNA-seq analysis for neural development study based on the hCO model. The approach can illuminate the complex mechanisms between oxygen and early neural development, offering insights into brain development and potential avenues for addressing neurodevelopmental disorders.

MATERIALS AND METHODS

Culture of hiPSCs

The feeder-free hiPSCs (409B2) were obtained from RIKEN BioResource Research Center (Ibaraki, Japan). Feeder-free hiPSCs were cultured on hESC-qualified Matrigel (354277, Corning, Corning, NY)–coated 35-mm dishes with Stemflex medium (A3349401, Thermo Fisher Scientific, Waltham, MA) and maintained in a 5% CO_2 incubator at 37°C. The culture and passage of the cells are performed following the procedures according to the manufacturer's instructions.

Lentiviral transduction

HiPSCs were transduced with lentiviral vector–mediated shRNA to silence the expression of *the NGB* gene. The *NGB* shRNA (*shNGB*) with the target sequence GTGATGCTCGTGATTGATGCT (TRCN0000059495), the shRNA scramble control *shLacZ* with the target sequence CGCGATCGTAATCACCCGAGT (TRCN 0000072224), and the *EGFP*-containing lentiviral vector (*pAS7w.EGFP.puro*) were obtained from the National RNAi Core Facility at the Academia Sinica, Taipei, Taiwan. To obtain stable *shNGB*, *shLacZ*, and *GFP* hiPSC lines, hiPSCs were plated in six-well plates (3516, Corning) at 40% confluence without antibiotics. For efficient transduction, the selected lentiviral vector was added into the fresh culture medium with 6 mM polybrene (Sigma-Aldrich, catalog no. H9268). The lentiviral-transduced hiPSCs were selected after the 48-hour transduction by incubating the cells in the selection medium containing puromycin (2 μg/ml) (Sigma-Aldrich, catalog no. P8833)

for 10 days, with the medium changed every other day. To confirm the efficiency of viral transduction, green fluorescent protein (GFP)–hiPSCs were used to form the cerebral organoids, and the GFP signal was found on most cells of organoids (fig. S6).

Cerebral organoid formation

Cerebral organoids were formed following well-established protocols with slight modification (*6*, *16*). The entire experimental timeline is illustrated in Fig. 1B. First, the colonized hiPSCs were gently dissociated into single-cell suspension using Accumax solution (A7089, Sigma-Aldrich Inc., St. Louis, MO). The cells were seeded into round-bottom ultralow attachment 96-well (7007, Corning) with a density of 12,000 cells per well to form embryoid bodies (EBs). The EBs were cultured in the AggreWell EB formation medium (05893, STEMCELL Technologies Inc., Cambridge, MA) that was supplied with the ROCK inhibitor Y-27632 (SCM075, Sigma-Aldrich) in a final concentration of 10 μM. After 6-day culture, the dorsal forebrain identity was induced by Sonic Hedgehog (SHH) inhibitor cyclopamine A with a concentration of 5 μM (239803, Sigma-Aldrich). In the meantime, the ventral forebrain identity was induced by the Wnt inhibitor IWP-2 with a concentration of 2.5 μM (I0536, Sigma-Aldrich) and SHH agonist SAG with a concentration of 100 nM (566660, Sigma-Aldrich). After the 6-day neural induction, a dorsal EB and a ventral patterning EB were embedded together within a single Matrigel droplet. The EB-containing droplets were cultured in an ultralow attachment 24-well plate (3473, Corning) with differentiation medium containing a 1:1 mixture of Dulbecco's modified Eagle's medium (DMEM)/F12 (12660012, Thermo Fisher Scientific) and neurobasal medium (21103049, Thermo Fisher Scientific) containing N2 supplement (17502048, Thermo Fisher Scientific) with a ratio of 1:200, B27 supplement without vitamin A (12587010, Thermo Fisher Scientific) with a ratio of 1:100, 550 μM 2-mercaptoethanol (1:3000) (21985023, Thermo Fisher Scientific), insulin (1:4000) (I9278, Sigma-Aldrich Inc.), GlutaMAX (1:100) (35050061, Thermo Fisher Scientific), and minimum essential medium non-essential amino acids (MEM-NEAA) (1:100) (11140-050, Thermo Fisher Scientific). After 4-day stationary growth, the culture medium was changed to the aforementioned differentiation medium above with modification of replacing the B27 supplement without vitamin A with the B27 supplement with vitamin A (1:200) (17504044, Thermo Fisher Scientific). The developing organoids were transferred to the orbital shaker until the collection date.

FD-FLIM measurement of intra-organoid oxygen tension

The FD-FLIM setup was constructed based on a commercially available inverted fluorescence microscope (DMI 6000B, Leica Microsystems, Wetzlar, Germany). In the setup, the microscope was equipped with high-power light-emitting diode (LED) (nominal wavelength: 470 nm, Thorlabs, Newton, NJ, catalog no. M470LP-C2) as a fluorescence excitation source and a dual-tap complementary metal-oxide semiconductor (CMOS) FLIM camera (PCO.FLIM, Excelitas Technologies Corp., Waltham, MA) as an imaging sensor. The LED and the camera were synchronized and modulated with a 50-kHz digital signal generated by the camera. A narrow band filter cube (AOR, Leica Microsystems) was used to acquire appropriate fluorescence signals emitted from the oxygen-sensitive fluorescence microbeads. The signal was then collected with a 5×, NA (numerical aperture) = 0.12 objective (N PLAN, Leica Microsystems) and finally recorded by the camera by passing through the filter cube.

For the intra-organoid oxygen tension measurement, 50-μm-diameter oxygen-sensitive fluorescence microbeads (CPOx, Colibri Photonics GmbH) were reconstituted in Dulbecco's phosphate-buffered saline (DPBS) (14190144, Thermo Fisher Scientific) containing 1% bovine serum albumin (BSA) (05470, Sigma-Aldrich) to a final concentration of 10 mg/ml. The solution was then premixed with liquid hydrogel at a ratio of 1:20 (v/v) on day 12, and the microbead-containing hydrogel was used for the fusion of the dorsal EB and the ventral patterning EB. The fluorescence intensity and lifetime of the beads (excitation wavelength: 420 to 490 nm, emission wavelength: 570 to 670 nm) were strongly reduced and shortened by the presence of molecular oxygen due to dynamic quenching. The oxygen concentration can be estimated from the lifetime variation according to the Stern-Volmer equation

$$\frac{\tau_0}{\tau} = 1 + K_q \times [O_2]$$

where τ_0 and τ are the fluorescence lifetimes without and with the presence of oxygen, respectively, and K_q is a quenching constant. The quenching constant was calculated from the calibration process described in the previous work (*45*). The FLIM image set of a droplet of an oxygen-sensitive fluorescent dye, 25 μM tris(4,7-diphenyl-1,10-phenanthroline) ruthenium(II) bis(perchlorate) [$Ru(dpp)_3(ClO_4)_2$; 75213-31-9, Toronto Research Chemicals, Ontario, Canada], with a known lifetime ($\tau = 1.185$ μs) was used as reference (*45*). As a result, the average lifetime and oxygen concentration of a CPOx microbead can be estimated. It is noted that the locations of the microbead were identified by a mathematics software program (MATLAB R2017a, MathWorks, Natick, MA) by thresholding the intensity of the image. The detailed characterization and analysis process was described in the previous literature (*45*).

Single-cell preparation, RNA sequencing, and analysis

On the collection date at days 24 and 35, the hCOs were washed with calcium and magnesium-free DPBS (14190144, Thermo Fisher Scientific) and incubated with Cell Recovery Solution (354253, Corning) to dissociate the polymerized Matrigel. The collected hCOs were cut into two to four small pieces using a scalpel and washed with the DPBS several times to remove the potential debris. Following the manufacturer's instruction, the pieces of the hCOs were disassociated into single-cell suspension through the Neural Tissue Dissociation Kit (130-092-628, Miltenyi Biotec, Bergisch Gladbach, German). After the DPBS wash, the remaining debris and clumps in the cell suspension were filtered through a 40-μm cell strainer (352340, Corning). The dissociated cells were stained with calcein AM (C1430, Thermo Fisher Scientific) to estimate cell viability. Only the batches with a viability greater than 80% would be exploited for further analysis. The single-cell suspension with a density of 1000 cells/μl was loaded into a single-cell analysis chip, Chromium Single Cell 3′ Chip G (PN-2000177, 10x Genomics, Pleasanton, CA), and processed through the chip controller to generate single-cell Gel Beads in Emulsion (GEMs). The scRNA-seq libraries were prepared with the Chromium Single Cell 3′ Library & Gel Bead Kit v.3.1 (PN-1000121, 10x Genomics). The constructed libraries were sequenced following the specific procedures (R1: 28 cycles, R2: 91 cycles, and i7 index: 8 cycles) by a sequencing system (NovaSeq 6000, Illumina, San Diego, CA).

The raw sequencing data were aligned to the GRCh38 human reference genome by the Cell Ranger pipeline v.6.1.2 (10x Genomics)

with default parameters to generate the cell-by-gene count matrix. The matrix data were further analyzed by the custom Python code with the preconfigured toolkit (Scanpy v1.8) (*46*). In brief, the processing data with fewer than 200 genes or more than 6000 total genes were filtered to remove empty droplets and potential doublets, respectively. Cells containing more than 5% mitochondrial reads, which indicate dead cells, were also excluded. The expression data were normalized with unique molecular identifier (UMI) reads for each cell and log-transformed. Next, we determined the highly variable genes of the count matrices and performed the principal components analysis (PCA) for dimensional reduction. The built-in function Leiden graph-clustering method (*47*) in Scanpy was used to calculate the UMAP coordinates for the presentation of the clustering identification. Clusters were annotated by literature-based marker genes (*7*, *23*) approved by the Wilcoxon rank sum test (*48*). The gene set list is as follows: (*FABP7*, *GLI3*, *SOX2*, *PAX6*, *VIM*, and *HES1*) for neural stem/progenitor cells, (*NEUROG2*, *EMX2*, *EOMES*, and *NEUROD1*) for basal progenitor cells, (*CCNB1*, *HMMR*, *MKI67*, and *ASPM*) for dividing cells, (*DLX2* and *ASCL1*) for interneuron progenitor cells, (*GAD1*, *DLX5*, and *SST*) for interneurons, (*DCX*, *SOX4*, *CD24*, *STMN2*, and *MAP2*) for differentiated neurons, and (*TBR1*, *SLC17A6*, *GRIN2B*, *STMN2*, and *MAP2*) for excitatory neurons. For integrated batch data, the built-in function "ingest" was applied to map the calculated data toward the reference data. The batch balanced *k* nearest neighbor (BBKNN) method (*49*) was used to correct the batch effect. For GSEA, the external EnrichR (*50*) of GSEApy package (*51*) was applied, and a specific library, "GO_Biological_Process_2021," was used to identify the potential biological functions of hCOs. The decoupler package (*52*, *53*) was applied, and the MSigDB (*30*) database was conducted to query the gene sets for matching the pathway activity.

Histology, cryosectioning, and immunofluorescence

The organoids were fixed by 4% paraformaldehyde (PFA) (158127, Sigma-Aldrich Inc.) at 4°C overnight. After fixation, the tissue was washed twice with DPBS and transferred into 30% sucrose (S0389, Sigma-Aldrich Inc.) overnight for cryoprotection. The tissue was immersed in an embedding solution containing 7.5% gelatin (G2500, Sigma-Aldrich Inc.) and 15% sucrose for 1 hour. Subsequently, the tissue was embedded into the mold with optimal cutting temperature (OCT) compound (3801480, Leica Biosystems, Deer Park, IL) for long-term storage at −80°C. The embedded organoids were sliced frozenly into 20-μm sections by cryostat microtome (CM3050S, Leica Microsystems). Tissue slices were mounted onto the silane-coated coverslips (5116, Muto Pure Chemicals, Japan).

Coverslips were washed with tris-buffered saline (TBS) containing 1% glycine (G8898, Sigma-Aldrich Inc.), 0.4% Triton X-100 (X100, Sigma-Aldrich Inc.), 3% BSA (A7906, Sigma-Aldrich Inc.), and 0.1% sodium azide (S8032, Sigma-Aldrich Inc.). For blocking the nonspecific binding sites, coverslips were incubated in a blocking buffer containing either 10% normal goat serum (31872, Thermo Fisher Scientific) or 10% normal donkey serum (D9663, Sigma-Aldrich Inc.) in TBS for 1 hour at room temperature. Subsequently, the coverslips were incubated with primary antibodies in species-appropriate combinations for 24 hours at 4°C. Primary antibodies and dilution used in our experiments included goat anti-SOX2 (1:300) (AF2018, R&D Systems Inc., Minneapolis, MN), mouse anti-TUBB3 (1:300) (MMS-435P, BioLegend, San Diego, CA), mouse anti–Ki-67 (1:250) (550609, BD Pharmingen, Franklin Lakes, NJ), rabbit anti-NESTIN (1:250) (ABD69, Merck Millipore, Temecula, CA), and rabbit anti-GFP (1:1000) (A6556, Abcam, Cambridge, UK).

Following incubation with primary antibodies, the coverslips were washed with TBS and subsequently incubated with secondary antibodies in a blocking buffer for 24 hours at 4°C. Secondary antibodies included Alexa 488, 546, 633–conjugated goat anti-mouse (A-11001, Thermo Fisher Scientific), anti-rabbit immunoglobulin G (IgG) (A-11035, Thermo Fisher Scientific), and donkey anti-goat IgG (A-21082, Thermo Fisher Scientific). The coverslips were washed with TBS and subsequently mounted with ProLong Gold anti-fade (P36930, Thermo Fisher Scientific). All the images were taken by LSM880 confocal microscopy (Zeiss GmbH, Oberkochen, Germany). The size, thickness, and cell number counting were estimated by an imaging analysis software, ImageJ (U.S. National Institutes of Health).

Supplementary Materials

This PDF file includes:

Figs. S1 to S6
Tables S1 to S7

REFERENCES AND NOTES

1. L. Sokoloff, S. S. Kety, Regulation of cerebral circulation. *Physiol. Rev. Suppl.* **4**, 38–44 (1960).
2. C. Lange, M. Turrero Garcia, I. Decimo, F. Bifari, G. Eelen, A. Quaegebeur, R. Boon, H. Zhao, B. Boeckx, J. Chang, C. Wu, F. Le Noble, D. Lambrechts, M. Dewerchin, C. J. Kuo, W. B. Huttner, P. Carmeliet, Relief of hypoxia by angiogenesis promotes neural stem cell differentiation by targeting glycolysis. *EMBO J.* **35**, 924–941 (2016).
3. A. Vasudevan, J. E. Long, J. E. Crandall, J. L. R. Rubenstein, P. G. Bhide, Compartment-specific transcription factors orchestrate angiogenesis gradients in the embryonic brain. *Nat. Neurosci.* **11**, 429–439 (2008).
4. R. C. Vannucci, Hypoxic-ischemic encephalopathy. *Am. J. Perinatol.* **17**, 113–120 (2000).
5. L. Wagenfuhr, A. K. Meyer, L. Braunschweig, L. Marrone, A. Storch, Brain oxygen tension controls the expansion of outer subventricular zone-like basal progenitors in the developing mouse brain. *Development* **142**, 2904–2915 (2015).
6. M. A. Lancaster, M. Renner, C.-A. Martin, D. Wenzel, L. S. Bicknell, M. E. Hurles, T. Homfray, J. M. Penninger, A. P. Jackson, J. A. Knoblich, Cerebral organoids model human brain development and microcephaly. *Nature* **501**, 373–379 (2013).
7. J. G. Camp, F. Badsha, M. Florio, S. Kanton, T. Gerber, M. Wilsch-Brauninger, E. Lewitus, A. Sykes, W. Hevers, M. Lancaster, J. A. Knoblich, R. Lachmann, S. Paabo, W. B. Huttner, B. Treutlein, Human cerebral organoids recapitulate gene expression programs of fetal neocortex development. *Proc. Natl. Acad. Sci. U.S.A.* **112**, 15672–15677 (2015).
8. Y. Tanaka, B. Cakir, Y. Xiang, G. J. Sullivan, I.-H. Park, Synthetic analyses of single-cell transcriptomes from multiple brain organoids and fetal brain. *Cell Rep.* **30**, 1682–1689.e3 (2020).
9. X. Qian, H. N. Nguyen, M. M. Song, C. Hadiono, S. C. Ogden, C. Hammack, B. Yao, G. R. Hamersky, F. Jacob, C. Zhong, K.-J. Yoon, W. Jeang, L. Lin, Y. Li, J. Thakor, D. A. Berg, C. Zhang, E. Kang, M. Chickering, D. Nauen, C.-Y. Ho, Z. Wen, K. M. Christian, P.-Y. Shi, B. J. Maher, H. Wu, P. Jin, H. Tang, H. Song, G.-L. Ming, Brain-region-specific organoids using mini-bioreactors for modeling ZIKV exposure. *Cell* **165**, 1238–1254 (2016).
10. P. Wang, R. Mokhtari, E. Pedrosa, M. Kirschenbaum, C. Bayrak, D. Zheng, H. M. Lachman, CRISPR/Cas9-mediated heterozygous knockout of the autism gene CHD8 and characterization of its transcriptional networks in cerebral organoids derived from iPS cells. *Mol. Autism.* **8**, 11 (2017).
11. A. M. Pasca, J.-Y. Park, H.-W. Shin, Q. Qi, O. Revah, R. Krasnoff, R. O'Hara, A. J. Willsey, T. D. Palmer, S. P. Pasca, Human 3D cellular model of hypoxic brain injury of prematurity. *Nat. Med.* **25**, 784–791 (2019).
12. J. Penney, W. T. Ralvenius, L. H. Tsai, Modeling Alzheimer's disease with iPSC-derived brain cells. *Mol. Psychiatry* **25**, 148–167 (2020).
13. M. S. Kim, D.-H. Kim, H. K. Kang, M. G. Kook, S. W. Choi, K.-S. Kang, Modeling of hypoxic brain injury through 3D human neural organoids. *Cells* **10**, 234 (2021).
14. O. S. Finikova, A. Y. Lebedev, A. Aprelev, T. Troxler, F. Gao, C. Garnacho, S. Muro, R. M. Hochstrasser, S. A. Vinogradov, Oxygen microscopy by two-photon-excited phosphorescence. *ChemPhysChem* **9**, 1673–1679 (2008).
15. T. V. Esipova, M. J. P. Barrett, E. Erlebach, A. E. Masunov, B. Weber, S. A. Vinogradov, *Oxyphor* 2P: A high-performance probe for deep-tissue longitudinal oxygen imaging. *Cell Metab.* **29**, 736–744.e7 (2019).

16. J. A. Bagley, D. Reumann, S. Bian, J. Levi-Strauss, J. A. Knoblich, Fused cerebral organoids model interactions between brain regions. *Nat. Methods* **14**, 743–751 (2017).
17. N. Horie, K. So, T. Moriya, N. Kitagawa, K. Tsutsumi, I. Nagata, K. Shinohara, Effects of oxygen concentration on the proliferation and differentiation of mouse neural stem cells in vitro. *Cell. Mol. Neurobiol.* **28**, 833–845 (2008).
18. M. C. Simon, B. Keith, The role of oxygen availability in embryonic development and stem cell function. *Nat. Rev. Mol. Cell Biol.* **9**, 285–296 (2008).
19. B. J. Molyneaux, P. Arlotta, J. R. L. Menezes, J. D. Macklis, Neuronal subtype specification in the cerebral cortex. *Nat. Rev. Neurosci.* **8**, 427–437 (2007).
20. A. Kriegstein, A. Alvarez-Buylla, The glial nature of embryonic and adult neural stem cells. *Annu. Rev. Neurosci.* **32**, 149–184 (2009).
21. J. H. Lui, D. V. Hansen, A. R. Kriegstein, Development and evolution of the human neocortex. *Cell* **146**, 18–36 (2011).
22. S. Islam, A. Zeisel, S. Joost, G. La Manno, P. Zajac, M. Kasper, P. Lonnerberg, S. Linnarsson, Quantitative single-cell RNA-seq with unique molecular identifiers. *Nat. Methods* **11**, 163–166 (2014).
23. J. Zhang, J. Jiao, Molecular biomarkers for embryonic and adult neural stem cell and neurogenesis. *Biomed. Res. Int.* **2015**, 727542 (2015).
24. M. Ashburner, C. A. Ball, J. A. Blake, D. Botstein, H. Butler, J. M. Cherry, A. P. Davis, K. Dolinski, S. S. Dwight, J. T. Eppig, M. A. Harris, D. P. Hill, L. Issel-Tarver, A. Kasarskis, S. Lewis, J. C. Matese, J. E. Richardson, M. Ringwald, G. M. Rubin, G. Sherlock, Gene ontology: Tool for the unification of biology. *Nat. Genet.* **25**, 25–29 (2000).
25. The Gene Ontology Consortium, The Gene Ontology resource: Enriching a GOld mine. *Nucleic Acids Res.* **49**, D325–D334 (2021).
26. A. Pesce, S. Dewilde, M. Nardini, L. Moens, P. Ascenzi, T. Hankeln, T. Burmester, M. Bolognesi, Human brain neuroglobin structure reveals a distinct mode of controlling oxygen affinity. *Structure* **11**, 1087–1095 (2003).
27. A. Fabrizius, D. Andre, T. Laufs, A. Bicker, S. Reuss, E. Porto, T. Burmester, T. Hankeln, Critical re-evaluation of neuroglobin expression reveals conserved patterns among mammals. *Neuroscience* **337**, 339–354 (2016).
28. T. Burmester, B. Weich, S. Reinhardt, T. Hankeln, A vertebrate globin expressed in the brain. *Nature* **407**, 520–523 (2000).
29. S. Cutrupi, G. Ferrero, S. Reineri, F. Cordero, M. De Bortoli, Genomic lens on neuroglobin transcription. *IUBMB Life* **66**, 46–51 (2014).
30. A. Liberzon, C. Birger, H. Thorvaldsdottir, M. Ghandi, J. P. Mesirov, P. Tamayo, The molecular signatures database hallmark gene set collection. *Cell Syst.* **1**, 417–425 (2015).
31. M. Knobloch, S. Jessberger, Metabolism and neurogenesis. *Curr. Opin. Neurobiol.* **42**, 45–52 (2017).
32. E. Fordel, L. Thijs, L. Moens, S. Dewilde, Neuroglobin and cytoglobin expression in mice. Evidence for a correlation with reactive oxygen species scavenging. *FEBS J.* **274**, 1312–1317 (2007).
33. J. Liu, Z. Yu, S. Guo, S.-R. Lee, C. Xing, C. Zhang, Y. Gao, D. G. Nicholls, E. H. Lo, X. Wang, Effects of neuroglobin overexpression on mitochondrial function and oxidative stress following hypoxia/reoxygenation in cultured neurons. *J. Neurosci. Res.* **87**, 164–170 (2009).
34. S. Raychaudhuri, J. Skommer, K. Henty, N. Birch, T. Brittain, Neuroglobin protects nerve cells from apoptosis by inhibiting the intrinsic pathway of cell death. *Apoptosis* **15**, 401–411 (2010).
35. Z. Yu, C. Cheng, Y. Liu, N. Liu, E. H. Lo, X. Wang, Neuroglobin promotes neurogenesis through Wnt signaling pathway. *Cell Death Dis.* **9**, 945 (2018).
36. R. I. Dmitriev, A. V. Zhdanov, Y. M. Nolan, D. B. Papkovsky, Imaging of neurosphere oxygenation with phosphorescent probes. *Biomaterials* **34**, 9307–9317 (2013).
37. K. Zhang, L. Zhu, M. Fan, Oxygen, a key factor regulating cell behavior during neurogenesis and cerebral diseases. *Front. Mol. Neurosci.* **4**, 5 (2011).
38. A. Fago, C. Hundahl, S. Dewilde, K. Gilany, L. Moens, R. E. Weber, Allosteric regulation and temperature dependence of oxygen binding in human neuroglobin and cytoglobin: Molecular mechanisms and physiological significance. *J. Biol. Chem.* **279**, 44417–44426 (2004).
39. Z. Yu, N. Liu, J. Liu, K. Yang, X. Wang, Neuroglobin, a novel target for endogenous neuroprotection against stroke and neurodegenerative disorders. *Int. J. Mol. Sci.* **13**, 6995–7014 (2012).
40. H. Wen, L. Liu, L. Zhan, D. Liang, L. Li, D. Liu, W. Sun, E. Xu, Neuroglobin mediates neuroprotection of hypoxic postconditioning against transient global cerebral ischemia in rats through preserving the activity of Na^+/K^+ ATPases. *Cell Death Dis.* **9**, 635 (2018).
41. M. Schmidt, A. Giessl, T. Laufs, T. Hankeln, U. Wolfrum, T. Burmester, How does the eye breathe? Evidence for neuroglobin-mediated oxygen supply in the mammalian retina. *J. Biol. Chem.* **278**, 1932–1935 (2003).
42. P. A. Roberts, E. A. Gaffney, P. J. Luthert, A. J. E. Foss, H. M. Byrne, Retinal oxygen distribution and the role of neuroglobin. *J. Math. Biol.* **73**, 1–38 (2016).
43. L. Shang, D. Mao, Z. Li, X. Gao, J. Deng, Neuroglobin is involved in the hypoxic stress response in the brain. *Biomed. Res. Int.* **2022**, 8263373 (2022).
44. B. Haines, X. Mao, L. Xie, S. Spusta, X. Zeng, K. Jin, D. A. Greenberg, Neuroglobin expression in neurogenesis. *Neurosci. Lett.* **549**, 3–6 (2013).
45. H.-M. Wu, T.-A. Lee, P.-L. Ko, W.-H. Liao, T.-H. Hsieh, Y.-C. Tung, Widefield frequency domain fluorescence lifetime imaging microscopy (FD-FLIM) for accurate measurement of oxygen gradients within microfluidic devices. *Analyst* **144**, 3494–3504 (2019).
46. F. A. Wolf, P. Angerer, F. J. Theis, SCANPY: Large-scale single-cell gene expression data analysis. *Genome Biol.* **19**, 15 (2018).
47. V. A. Traag, L. Waltman, N. J. van Eck, From Louvain to Leiden: Guaranteeing well-connected communities. *Sci. Rep.* **9**, 5233 (2019).
48. C. Soneson, M. D. Robinson, Bias, robustness and scalability in single-cell differential expression analysis. *Nat. Methods* **15**, 255–261 (2018).
49. K. Polanski, M. D. Young, Z. Miao, K. B. Meyer, S. A. Teichmann, J.-E. Park, BBKNN: Fast batch alignment of single cell transcriptomes. *Bioinformatics* **36**, 964–965 (2020).
50. M. V. Kuleshov, M. R. Jones, A. D. Rouillard, N. F. Fernandez, Q. Duan, Z. Wang, S. Koplev, S. L. Jenkins, K. M. Jagodnik, A. Lachmann, M. G. McDermott, C. D. Monteiro, G. W. Gundersen, A. Ma'ayan, Enrichr: A comprehensive gene set enrichment analysis web server 2016 update. *Nucleic Acids Res.* **44**, W90–W97 (2016).
51. Z. Fang, X. Liu, G. Peltz, GSEApy: A comprehensive package for performing gene set enrichment analysis in Python. *Bioinformatics* **39**, btac757 (2023).
52. D. Turei, A. Valdeolivas, L. Gul, N. Palacio-Escat, M. Klein, O. Ivanova, M. Olbei, A. Gabor, F. Theis, D. Modos, T. Korcsmaros, J. Saez-Rodriguez, Integrated intra- and intercellular signaling knowledge for multicellular omics analysis. *Mol. Syst. Biol.* **17**, e9923 (2021).
53. P. Badia-i-Mompel, J. Velez Santiago, J. Braunger, C. Geiss, D. Dimitrov, S. Muller-Dott, P. Taus, A. Dugourd, C. H. Holland, R. O. Ramirez Flores, J. Saez-Rodriguez, decoupleR: Ensemble of computational methods to infer biological activities from omics data. *Bioinform. Adv.* **2**, vbac016 (2022).

Acknowledgments: We would like to thank the RNA Technology Platform and Gene Manipulation Core Facility (RNAi core) of the National Core Facility for Biopharmaceuticals at Academia Sinica in Taiwan for providing shRNA reagents and related services. **Funding:** This work was supported by the National Science and Technology Council (NSTC) Taiwan (grant 110-2221-E-001-005-MY3 to Y.-C.T.), Academia Sinica Career Development Award (grant AS-CDA-106-M07 to Y.-C.T.), and Academia Sinica Neuroscience Core Facility (grant AS-CFII-110-101 to Y.-J.C.). **Author contributions:** All authors reviewed the manuscript. Conceptualization: Y.-H.L., M.-T.C., C.-C.H., and Y.-C.T. Methodology: Y.-H.L., M.-T.C., C.-C.H., H.-M.W., and Y.-C.T. Investigation: Y.-H.L., M.-T.C., H.-C.L., T.-A.L., Y.-J.C., C.-C.H., and H.-M.W. Visualization: Y.-H.L., C.-C.H., H.-M.W., and Y.-C.T. Supervision: Y.-C.T. Writing—original draft: Y.-H.L., M.-T.C., and Y.-C.T. Writing—review and editing: Y.-H.L., M.-T.C., C.-C.H., H.-M.W., and Y.-C.T. Resources: Y.-H.L., M.-T.C., H.-C.L., Y.-J.C., C.-C.H., H.-M.W., and Y.-C.T. Data curation: Y.-H.L., C.-C.H., H.-M.W., and Y.-C.T. Validation: Y.-H.L., M.-T.C., C.-C.H., H.-M.W., and Y.-C.T. Formal analysis: Y.-H.L., H.-M.W., and Y.-C.T. Software: Y.-H.L., M.-T.C., and H.-M.W. Project administration: Y.-H.L. and Y.-C.T. Funding acquisition: Y.-J.C. and Y.-C.T. **Competing interests:** The authors declare that they have no competing interests. **Data and materials availability:** RNA sequencing data are available on the Gene Expression Omnibus (GEO accession number: GSE253940), and all other data needed to evaluate the conclusions in the paper are present in the paper and/or the Supplementary Materials.

Submitted 27 January 2024
Accepted 5 February 2025
Published 12 March 2025
10.1126/sciadv.ado1164